Constrained snake vs. conventional snake for carotid ultrasound automated IMT measurements on multi-center data sets

Constrained Snake vs. Conventional Snake for Carotid Ultrasound Automated IMT Measurements on Multi-Center Data Sets

Filippo Molinari[1], PhD; Kristen M. Meiburger[1], MSc; Luca Saba[4], MD;

U. Rajendra Acharya[3], PhD; Mario Ledda[4], MD;

Andrew Nicolaides[5], (Hon.) PhD; Jasjit S. Suri[6], PhD, MBA, Fellow AIMBE

[1] *Biolab, Department of Electronics, Politecnico di Torino, Torino, Italy*

[3] *Dept ECE, Ngee Ann Polytechnic, Singapore, Singapore*

[4] *Department of Radiology, A.U.O. Cagliari, Cagliari, Italy*

[5] *Vascular Diagnostic Center, Nicosia, Cyprus*

[6] *CTO Global Biomedical Technologies, Roseville, CA, USA and Research Professor (Aff.) Idaho State University, Pocatello, ID, USA*

Corresponding Author:

Prof. Filippo Molinari, PhD

BioLab – Department of Electronics, Politecnico di Torino

Corso Duca degli Abruzzi 24, 10129 Torino, Italy

Phone: +39 (0)11 564 4135

Fax: +30 (0)11 564 4217

Email: filippo.molinari@polito.it

Abstract

Accurate intima-media thickness (IMT) measurement of the carotid artery from minimal plaque ultrasound images is a relevant clinical need, since IMT increase is related to the progression of atherosclerosis.

In this paper, we describe a novel dual snake-based model for the high-performance carotid IMT measurement, called CMUDS (Carotid Measurement Using Dual-Snakes). Snakes (which are deformable contours) adapt to the lumen-intima (LI) and media-adventitia (MA) interfaces, thus enabling the IMT computation as distance between the LI and MA snakes. However, traditional snakes might be unable to maintain a correct distance and in some spatial location along the artery, it might even collapse between them or diverge. The technical improvement of this work is the definition of a dual snake-based constrained system, which prevents the LI and MA snakes from collapsing or bleeding, thus optimizing the IMT estimation.

The CMUDS system consists of two parametric models automatically initialized using far adventitia border which we automatically traced by using a previously developed multi-resolution approach. The dual snakes evolve simultaneously and are constrained by the distances between them, ensuring the regularization of LI/MA topology. We benchmarked our automated CMUDS with the previous conventional semi-automated snake system called CMUSS.

Two independent readers manually traced the LIMA boundaries of a multi-institutional, multi-ethnic, and multi-scanner database of 665 CCA longitudinal 2D images. We evaluated our system performance by comparing it with the gold standard as traced by clinical readers.

CMUDS and CMUSS correctly processed 100% of the 665 images. When compared the performance with respect to two readers, our automatically measured IMT was on average very close to that of the two readers (IMT measurement biases for CMUSS was equal to -0.011±0.329 mm and -0.045±0.317 mm, respectively, while for CMUDS, it was 0.030±0.284 mm and -0.004±0.273 mm, respectively). The Figure-of-Merit of the system was 98.5% and 94.4% for

CMUSS, while 96.0% and 99.6% for CMUDS, respectively. Results showed that the dual-snake system CMUDS reduced the IMT measurement error accuracy (Wilcoxon, $p < 0.02$) and the IMT error variability (Fisher, $p < 3\ 10^{-2}$).

We propose the CMUDS technique for use in large multi-centric studies, where the need for a standard, accurate, and automated IMT measurement technique is required.

Keywords: atherosclerosis, carotid intima-media thickness, deformable parametric model, snake, constraints, first-order absolute moment, automation, validation, accuracy, reproducibility.

1. Introduction

This paper describes development of the clinically relevant approach allowing improved determination of intima-media thickness (IMT) of the carotid arteries.

Recently, the data from the World Health Organization (1) indicated that cardiovascular diseases account from one-third of all the global deaths in Western countries. The World Health Organization also estimated that by 2040 the cardiovascular diseases would account for 50% of all global deaths, including also emerging countries and third world countries (1). Atherosclerosis is the earliest manifestation of the onset of a cardiovascular disease. Atherosclerosis is defined as the degeneration of the arterial wall, with consequent deposition of lipids, calcium, and other blood-borne materials within the arterial wall itself. This process was documented in several studies about the genesis and progression of atherosclerosis (2-4).

In the multi-centric Rotterdam study, the intima-media thickness of the carotid arteries was found to be a predictor of cardiovascular risk (5). Carotid IMT was also associated to the incidence of several cardiovascular diseases, as documented by other large clinical studies (6-10). The accurate measurement of the IMT from ultrasound images is, therefore, clinically very important for the assessment of the risk factor of the patients and for screening purposes.

In clinical practice, the IMT is usually measured by expert sonographers on longitudinal B-Mode images. By means of the scanner caliper, the sonographer places two markers in correspondence of the lumen-intima (LI) and of the media-adventitia (MA) interfaces. The distance between the two markers is the estimation of the IMT. This process introduces variability in the results, which is linked to the sonographers experience. In a recent study, Polak *et al.* showed (11) that when different trained sonographers manually measured the IMT, a difference of 0.21 mm was observed (since the average value of the IMT of atherosclerotic patients is about 0.9 mm, the difference was about 23% of the nominal value). This inter-reader variability could lead to an incorrect assessment of the patients' risk assessment. Hence, computer methods aiding the IMT

measurement find their utility in order to reduce the measurement variability while maintaining the measurement precision.

Touboul *et al.*, who were the first to propose a computer method to aid the IMT measurement (12) and used it in the epidemiological PARC study (13), which was focused on the assessment of carotid IMT measurement reproducibility. The results of the PARC study revealed the need for a computer system capable of measuring the IMT with a low error (compared to manual tracings by experts). Touboul *et al.* obtained an IMT measurement error equal to 0.0185 mm. This study was one of the first proposing a computer system for the IMT measurement in multi-centric studies (*i.e.*, in studies where images are collected by different physicians in different Institutions, which usually capture images using different ultrasound equipments).

Hence, computer methods aiding the IMT measurement find their utility in order to reduce the measurement variability while maintaining the measurement precision. When the LI and MA interfaces are traced by an image processing algorithm, the process is called "segmentation". In 2010, Molinari *et al.* (14) revised all the most used computer techniques for the carotid wall segmentation and IMT measurement. In this work, we benchmarked our innovative Dual Snake paradigm for the carotid LIMA automated segmentation and IMT measurement. We called this novel system as CMUDS (Carotid Measurement Using Dual Snake, a patented technology by Global Biomedical Technologies, CA, USA under the class of AtheroEdge™ systems). To fully appreciate the rationale of our choice and innovation, we would like to briefly revise the previous proposed solutions for computer-based IMT measurement. The most used image processing techniques for LIMA tracings and IMT measurement can be subdivided into:

1. edge-based and gradient-based methods (15-19);
2. dynamic programming and modeling methods (20-24);
3. analysis techniques based on specific distributions (*e.g.*, Nakagami, Hough) (25-27);
4. parametric deformable models (*i.e.* snakes) (28-30).

The principal advantage of standalone edge-based methods is the fast computation. In fact, edge detection can be performed by simple operations such as the high pass filtering of the image. These operations are very effective and the overall time required to high pass filter a B-Mode image is less than 0.5 ms. The principal drawback of edge-based methods is their sensitivity to noise because they are based on image differentiation. In fact, since edge detectors search for intensity variations, noise can lead to false edge detections and false edges.

The dynamic programming techniques are based on the minimization of a cost function, which derives from the image features. Cost terms and cost functions (in some algorithms up to 20 among terms and function were defined (21)) are related to physical characteristics of the image such as the pixel density. Since in ultrasounds the image characteristics depend on the scanner and on the settings, dynamic programming techniques are difficult to use in a multi-centric scenario, where images might come from different Institutions and different equipments.

The segmentation methods that model the carotid wall boundaries usually consider predetermined intensity features or shapes. Among all the intensity distributions, the Nakagami distribution (25) models the sequence of low intensity (*i.e.,* the carotid lumen), medium intensity (*i.e.*, the intima and media layers), and the high intensity (*i.e.*, the adventitia layer). The model can be accurate only if the overall intensities associated to layers do not change. Thus, the methods based on intensity distributions could not recognize the layers' intensities correctly if different scanners are adapted in acquisition protocol. The image transforms, such as the Hough transform (26), are used to detect specific shapes in an image. For example, Golemati *et al.* (26) used the Hough transform to detect the lines associated to the LI and MA interfaces profiles. However, this method can only process images where the LIMA interfaces are straight horizontal lines and therefore, this is a limitation. This strategy poses a challenge to curved arteries or inclined arteries.

The snake-based techniques have two major advantages:

- They are versatile because they can adapt to almost any carotid morphology. Since snakes are deformable curves, they can assume different shapes, and so they can correctly recognize the interfaces of straight, inclined, and curved carotids.
- They maintain a smooth shape of the LIMA profiles. This is clinically important, because, from a physiological point of view, the profiles of the wall layers are always regular and not disconnected.

Snakes, however, suffers also from two major drawbacks:

- *Need for initialization*: Snakes are dynamic contours, which evolve (or change) from an initial shape and converge (settle down at correct stable position) over time. Therefore, the contour has to be created (initialized) before convergence happens. It has been shown that the initialization influences the final segmentation (31). This happens because, once initialized, the snakes evolve while following the intensity changes in the image. Hence, clearly, the location of the snake initialization is important for the final result.
- *Sensitivity to noise*: This is because the snake is attracted by image discontinuities. As we have already discussed, intensity discontinuities are usually measured by using gradients. However, as mentioned above, gradients are noise sensitive. In carotid ultrasound images, there are different noise sources, the principal are: blood rouleaux and hypoechoic appearance of the LIMA interfaces due to lack of gel on the skin or incorrect insonation angle.

In last years, many snake-based techniques were proposed for the IMT measurement of the carotid arteries. Delsanto *et al.* proposed a completely automated snake-based technique, where the snake initialization was performed after having detected the carotid lumen (29, 32). Loizou *et al.* proposed to normalize the image intensity in order to allow the snake to correctly recognize the LIMA boundaries even when the interfaces had different brightness (30). Cheng *et al.* observed that sometimes the snake got trapped in-between the LI and the MA boundary. They proposed a new

model that prevented trapping (28) approximating the image discontinuities by using the Macleod Operator. In fact, the major problem of the snake-based techniques is the incorrect positioning of either the LI or the MA (or even both) snakes with respect to the actual interface. Often, this is due to the image gradients that are weak or noisy in correspondence of the LIMA boundaries, so that the snakes cannot properly follow the interfaces. If the snakes become too close, the IMT is underestimated, because the two snakes are too close than the actual carotid wall boundaries. We call this error condition as "collapsing". If the snakes are too far, the IMT is overestimated. We call this error condition ad "bleeding", meaning that the two snakes went too far away one from the other. Bleeding and collapsing of the LIMA snakes, therefore, are the major causes of incorrect IMT measurement.

The herein presented snake system is completely innovative and the main technical improvement of CMUDS is its constrained model, where the LI and the MA snakes are subjected to a mutual constrain, whose main objective is to prevent collapsing or bleeding. Snakes, when used as deformable techniques, are usually initialized close to LIMA interfaces. They must then evolve until they converge to the actual shape (as close as possible to the delineations by readers such as ultrasound sonographer or vascular surgeon). In the image processing technique we developed, this profile generation is totally automated, meaning that carotid artery recognition, far adventitia detection, region of interest estimation, initialization of the snakes, snake evolution, and final convergence are all carried out without any intervention by the user. We benchmarked CMUDS against traditional snake model having no constraints as proposed by Loizou *et al.* (30) (which we called CMUSS – Carotid Measurement Using Single Snake). We validated CMUDS on a multi-institutional, multi-ethnic, and multi-scanner database of 665 longitudinal carotid B-Mode images. In the following, we describe our methodology, benchmarking strategy, acquisition details on our image data sets, validation protocol, and the performance metrics adapted.

2. Materials and Methods

2.1 Constrained Dual Snake Energy Formulation

In this section we describe the automated CMUDS system. It consists of three cascaded steps: Step-I is the automate carotid recognition and tracing of the far adventitia wall (AD_F); Step-II is the ROI determination followed by initialization of two snake models (one for the LI interface and one for the MA); Step-III is the convergence and final LIMA tracing. Figure 1 shows a flow-chart of the CMUDS architecture, and is described step-by-step in the following. First of all, the input image was automatically cropped: the black frame border which usually surrounds the ultrasound B-Mode image was automatically removed by using either vendor-specific information (embedded in the DICOM formatted image) or by using a gradient-based approach (33).

2.1.1 Step-I: Carotid recognition and far adventitia wall tracing

Figure 2 depicts the AD_F recognition strategy. The AD_F profile was automatically traced by means of a recognition system based on first-order Gaussian filtering and multi-resolution approach (23, 34) (which we named as CAMES and that is fully described in the work by Molinari *et al.* (in press)).

The original image (fig. 2.a) is down-sampled by a factor of 2 (fig. 2.b) by using a bi-cubic interpolation as suggested by Zhen *et al.* (35). The multi-resolution method prepares the vessel wall's edge boundary such that the vessel wall thickness tends to be equivalent to the scale of the Gaussian kernels. The image is then filtered in order to reduce the speckle (fig. 2.c). We used a first-order statistics filter, which was suggested by Loizou *et al.* (36). They proved that this filter attenuated speckle without blurring the wall interfaces. The despeckled image was then filtered by a first-order derivative Gaussian kernel. The scale parameter of the kernel (*i.e.*, the value of σ) was chosen to be equal to the theoretical size of the carotid wall. Since our images database comprised

both normal and pathological subjects, we considered an average IMT value of 1 mm, which we converted in pixels. Hence, the scale parameter of the first-order Gaussian kernel was equivalent to 1 mm. As an example, for the images having a pixel density of 16 pixels/mm, the IMT nominal value scaled to half its size was 8 pixels, and this was the scale parameter of the first-order derivative Gaussian kernel. The effect of the first-order Gaussian filtering is shown in fig. 2.d, where the two bright stripes represent the carotid near and far wall position. This filtered image was considered column-by-column. The intensity profile of a column is shown in fig. 2.e. This profile was scanned starting from the bottom of the image (*i.e.*, from the point with the higher row index). The AD_F was defined as the farthest white point (*i.e.*, with intensity equal to 255 in a 0-255 gray scale) belonging to a white segment of at least 1 mm. This because, as we described earlier, the scale parameter of the first-order Gaussian kernel was chosen equal to 1 mm, thus the far wall should have a minimum size of 1 mm. The sequence of all the detected AD_F points constituted the final adventitia profile (fig. 2.f). This procedure has the advantage of being tuned to the size of the carotid wall, thereby attenuating the contribution coming from all the other image features (*i.e.*, underlying tissues, blood rouleaux streams, artifacts). Also, the value of σ is very easy to derive from the pixel density.

2.1.2 Step-II: Lumen-intima and Media-adventitia snakes initializations

The AD_F profile was then used for ROI reconstruction and initialize of snakes. The LI snake was initialized by shifting the AD_F profile 3 mm upwards. Let's call this value as Δ_{LI}. Since the maximum IMT value we had in our database was about 1.7 mm, a Δ_{LI} equal to 3 mm ensured that the LI snake was placed into the carotid lumen. The MA snake was initialized by shifting upwards the AD_F profile of a value Δ_{MA} equal to 0.1 mm. This value was the optimal choice to place the initial MA snake close to the interface without placing it in-between the LI and the MA boundaries. Fig. 3 shows samples of the AD_F and the snake initializations.

2.1.3 Step-III: CMUDS snake model and its convergence

A 2-D parametric deformable model (snake) is a mathematical description of a contour evolving on the image and driven by two energy types. The first type is the *Internal energies that* impose geometrical constraints on the contour. For example, an internal energy could limit the curvature as well as length of the snake. Hence, these internal energies are used for sharing and smoothing the contour. When snakes are used to segment the LI and MA interfaces, the internal energies can be used for smoothing the snakes, so that they can correctly adapt to the actual wall interfaces. The second type is the External energies, which are used to attract the snake in correspondence to the image discontinuities. Convergence is reached when the points of the snake are in correspondence of the image discontinuities (i.e., in this specific case, in correspondence of the lumen-intima and media-adventitia intensity transitions) and the internal forces counterbalance the external ones.

From a mathematical point of view, let $v(s)$ represent the snake, a 2D contour, where the parameter *s* is the curvilinear coordinate on the image. The curvilinear coordinate *s* is space-normalized in the range [0,1]. Each snake is associated and defined with an energy functional, constituting the internal and external energies. This energy functional is very important for a snake. This is because the snake reaches convergence when the energy functional is minimized. Therefore, when the energy associated to the snake is at its minimum, the internal and external forces counterbalance each other and the snake is stable. The energy functional we defined for our snake model $v(s)$ is the following:

$$E(v(s)) = \int_0^1 \alpha \left|v'(s)\right|^2 + \beta\, e(v(s)) + \gamma \left|v(s) - e(v(s))\right| ds \qquad (1)$$

In eq. (1), the internal energy E_i consists of the first term:

$$E_i(v(s)) = \int_0^1 \alpha \left|v'(s)\right|^2 ds \qquad (2)$$

Whereas the external energy E_e is:

$$E_e\left(v(s)\right) = \int_0^1 \beta\, e\left(v(s)\right) + \gamma \left| v(s) - e\left(v(s)\right)\right| ds \qquad (3)$$

The internal energy is used to constrain the shape of the contour and its properties. The parameter α is used to control the continuity, where $v'(s)$ is the first-order derivative of the snake curve $v(s)$. Dimensionally, the term $v'(s)$ is a velocity, ad hence the square modulus is used to model the associated energy (exactly as in physics the kinetic energy is associated to the square value of the velocity).

The external energy is used to attract the snake towards the image discontinuities. The first term of the external energy $\beta\, e\left(v(s)\right)$ is used in capturing the LIMA interface of the far wall. In fact, the functional $e(x,y)$ is an edge operator called FOAM (First Order Absolute Moment), which was proposed by Demi *et al.* (37) and adapted by Faita *et al.* for detection of the LIMA edges (15). The mathematical details of FOAM are summarized in the Appendix. To summarize, the FOAM operator is used to enhance the intensity transitions (such as those along the LIMA edges). Hence, FOAM assumes a high value in intensity transitions and it is zero valued in image regions characterized by a constant or uniform intensity. Unlike traditional image gradients, the FOAM operator is shown to be more robust with respect to noise. The basic concept of the FOAM operator is the application of a high pass filter after the image has been filtered by a Gaussian low pass filter. This joint filtering operation ensured the preservation of the intensity changes combined to noise smoothing. Figure 4 shows an example of FOAM: fig. 4.a is relative to the original B-Mode image, fig. 4.b to the corresponding FOAM map.

This first term of the external energy acts as a stopping function: when the snake points are in correspondence to the image edges, this energy has a high weight and therefore the points tend to be blocked there. The parameter β controls the strength of this stopping force.

It must be noted that this energy term $\beta\, e\big(v(s)\big)$ is null when the snake points are placed far from the edges, where the FOAM operator is equal to zero. Therefore, we added a second term of external energy to our deformable model. The second term of the external energy $\gamma \left|v(s) - e\big(v(s)\big)\right|$ models an attraction term, which attracts the snake points when they are far from the actual wall interfaces. This term computes the distance (*i.e.*, the difference) between the edges $e(x,y)$ of the image and the snake position. Therefore, even if the snake is placed in a region where the FOAM is null, it is attracted by the closest edge of the FOAM itself, with an attraction force that is proportional to the distance of the snake from the edge. This term is always positive when the snake is far from the edges, whereas it becomes zero valued when the snake is found in correspondence to the edges. The joint action of the two components of the external energy attracts the snake to the edges and locks the snake once it has reached its stable position (i.e., when the snake points have reached the actual wall interfaces).

In our segmentation problem, we had a total of six parameters: three for the LI snake (α_{LI}, β_{LI}, and γ_{LI}) and three for the MA snake (α_{MA}, β_{MA}, and γ_{MA}). Table 1 summarizes the parameter values. We chose the parameter values after pilot tests on a reduced subset of 20 images randomly selected from our database (results not reported here). We selected the parameters values that minimized the IMT measurement error on the 20 testing images. We had to impose different parameters for the LI and the MA snake because, like Faita *et al.* (15) pointed out, the LI and MA edges have different intensities in the FOAM edge map. Table 1 reports the variation range for the CMUDS parameters. As observed empirically, we defined those ranges as the numerical intervals in which the IMT measurement error did not change beyond 1%, with the change in dual snake parameters in the given interval. As it can be noticed, CMUDS was very robust, because variation as large as 20% did not cause a performance decrease higher than 1%. This was mainly due to the distance constraints in dual snakes.

Table 1 – Parameters value for the LI and MA snakes. Such values are same for all the images of the database.

LI/MA Snake	α (curvature)	β (stopping energy)	γ (attraction energy)
LI snake	0.5	0.1	0.1
Range	[0.4 – 0.6]	[0.08 – 0.15]	[0.01 – 0.2]
MA snake	0.5	0.2	0.05
Range	[0.4 – 0.6]	[0.1 – 0.3]	[0.03 – 0.06]

We also introduced a mutual constraint that forced the snakes to maintain a constrained distance from one other. This term was very important during convergence, because it prevented the snakes from bleeding or collapsing. We measured the distance between each point of the LI snake (called $v_{LI}(s)$) and the line segments of the MA snake (called $v_{MA}(s)$). We used the Polyline distance (PDM) as distance metric (38). Let's call this distance as $D_{LI\text{-}MA}$. We also measured the distance between the points of the MA snake and the line segments of the LI snake and called the distance as $D_{MA\text{-}LI}$. When we observed that one point of the LI snake $v_{LI}(s)$ had a distance higher than 3 mm or lower than 0.3 mm (which we considered as a bottom threshold for IMT) from $v_{MA}(s)$, we shifted that point up or down until its $D_{LI\text{-}MA}$ value was within the imposed constraints. The same correction was applied to the points of the MA snake $v_{MA}(s)$.

Once automatically initialized, the snakes evolved (without any interaction by the operator) according to the internal and external energies they were subject to. At each iteration step, we computed the coordinates of the snake points. When we observed that both the snakes had stopped evolving, we stopped the iteration and the shape of the snake was considered as the LIMA computer generated profiles. To avoid being trapped in a loop, we set a maximum limit on the number of iterations (called I_{MAX}). In this study, we set I_{MAX} equal to 200. We chose this value after pilot tests. We observed that in 100 iterations, the snakes could cover up to 0.8 mm distance. This was

compatible with our need, since the LI profile was initialized, on average, about 0.2±0.08 mm from the actual LI interface. Therefore, we set I_{MAX} equal to 200, which is double the value we tested, in order to ensure convergence in every condition.

2.2 Carotid Measurement Using Single Snake

We adapted the technique proposed by Loizou *et al.* (30, 39, 40) since it was the best performing and established snake-based technique for LIMA segmentation and IMT measurement. This technique showed an IMT measurement error as low as 0.050 ± 0.025 mm. This is a semi-automated method since it uses manual method for initialization of LIMA borders. This means the snake for LI is independently evolving to snake of MA. Thus we call it single snake method or CMUSS. We use CMUSS for benchmarking CMUDS. CMUSS consists of two steps: the first one (Step-I) is devoted to image pre-processing and snake initialization, whereas the second (Step-II) is the snake-based LIMA segmentation.

2.2.1 Step-I: Image preprocessing and snake initialization

Step-I of CMUSS requires human intervention: the operator selected a ROI containing the distal carotid wall. In CMUSS, all the images were first intensity normalized so that blood was represented by a gray level 0-5 and adventitia 180-190 (30, 40). Then, the preprocessing procedure, which took to the LI snake initialization, was the following (30):

- The image (considered in the manually traced ROI – fig. 5.A) was despeckled by using a linear scaling filter (called as *lsmv* by the Loizou *et al.* (36)) of 7x7 size. The filter was applied iteratively 5 times (36) (fig. 5.B), because Loizou *et al.* showed that this was the number of iterations required to attenuate speckle without decreasing the intensity of the LIMA interfaces.

- The despeckled image was binarized (fig. 5.C). The Otsu's criterion was used to automatically choose the proper threshold (41). Pixels belonging to the carotid wall should be mapped to white and other pixels to black.
- Image dilation by a 3x3 circular structuring element (fig. 5.D). This operation was needed in order to fill possible holes in the white region of fig. 5.C.
- Connected components analysis of the dilated image by considering 8-adjacents pixels (fig. 5.E). Labelling connected components was used to remove erroneous small edges that might trap the snake. Image segments smaller than 20 pixels were removed.
- Final image gradient (fig. 5.F) and extraction of the initial LI profile.

The LI contour was displaced of about 1 mm in order to create the MA initial contour. This value of 1 mm was chose since it represented the gross mean IMT value over our image set.

2.2.2 Step-II: CMUSS formulation and convergence

The CMUSS system was based on the Williams and Shah method (42). The energy functional associated to this snake is the following (defined in (30)):

$$E(v(s)) = \int_0^1 \alpha(s)E_{cont} + \beta(s)E_{curv} + \gamma(s)E_{image}ds \tag{4}$$

Where:

- $\alpha(s)E_{cont}$ is a contribute of internal energy, which is proportional to the first derivative of the snake $v(s)$. Being proportional to the derivative of the snake contour, this internal energy constrains the continuity of the snake. In the original formulation of Williams and Shah (42), this term was named "tension", meaning that the higher the values of α the higher was the tension of the snake (and, thus, the lower was its capacity of assuming curved shapes).

- $\beta(s)E_{curv}$ is a contribute of internal energy, which is proportional to the second-order derivative of the snake $v(s)$. Williams and Shah (42) named this term "stiffness", meaning that the higher the value of β, the stiffer the snake. This energy term controls the bending of the snake.
- The external energy $\gamma(s)E_{image}$ represents the image energy computed using the image gradient (30). As we already described, the gradients highlight the intensity changes in the image, so they are used to drive the snake towards such changes (in our segmentation problem, the intensity changes are the LIMA interfaces of the far carotid wall).

According to Loizou *et al*. (30), we have chosen in our study the initial values as: $\alpha_i(s) = 0.6$, $\beta_i(s) = 0.4$, and $\gamma_i(s) = 2$, to start the snake deformation, and these values are consistent with other previous snake-based models (30, 40, 42). For the segmentation of the LI and MA interfaces, we first segmented the image at the far wall of the CCA, by extracting the LI interface and then the MA interface using the proposed snake algorithm (30). We kept the maximum numbers of iterations I_{MAX} equal to 200 also for the CMUSS system.

2.3 Image database, performance assessment, and statistics

We tested CMUDS and CMUSS on a database of 665 longitudinal B-Mode images. This database is multi-institutional, multi-ethnic, multi-scanner, and multi-operator. It also comprised healthy and pathologic carotids. Table 2 reports the details of the acquired images, along with the pixel density and the ultrasound scanner used. All the patients signed an informed consent prior of undergoing the ultrasound examination. Each Institution took care of obtaining approval for the data acquired by the respective Ethical Committee or Institutional Review Board (IRB). The five image datasets were acquired independently from each Institution and in different years (the years in which images were acquired are reported by the first row of Table 2). Hence, no standardization was made among the five sets. Also, each sonographer adjusted the scanner settings (TGC values and gain factors) for

each corresponding patient during acquisition. All images were discretized at 8 bits (256 gray levels) and were provided in a digital form.

Table 2 – Patients demographics and ultrasound acquisition parameters. The references in the second row are relative to previous publications in which the specific set of images was used. (CF – conversion factor)

	Torino (’02-’09)	Nicosia (’02)	Cagliari (’09)	Porto (’08)	Hong Kong (’10-’11)
Total images	200	100	42	23	300
CF (mm/px)	0.0625 (32)	0.0600 (43)	0.0789 (44)	0.0900 (45)	0.0585
Patients	150	100	21	23	50
Age (years)	69 ± 16 (50-83)	54 ± 24 (25-95)	68 ± 8 (59-81)	[Not pub.]	60±5 (54-67)
Scanner	ATL HDI 5000	ATL HDI 3000	Esaote MyLab 70	ATL HDI 5000	Siemens Antares

An expert vascular radiologist and a neurosonographer manually segmented all the images by tracing the LI and MA profiles using ImgTracer™ (Global Biomedical Technologies, Inc., CA, USA) (46). The manual segmentations were considered as ground truth for computing the system performance of the computer-generated LIMA segmentations and IMT measurements. The first reader will be indicated as Reader-1 in the following, the second as Reader-2.

We used the Wilcoxon signed rank test to assess the difference between the average IMT measurement values, as suggested in previous similar studies (47). We choose the Wilcoxon test because it is a paired test, meaning that it is suitable to comparing two different measurement sets

made on the same images. We preferred the Wilcoxon test with respect to the Student's t-test because we could not assume that our values were normally distributed. To test the difference between the IMT measurement variances, we used the Fisher's F-test, which is the most commonly used statistical test to assess the equality of the variances of two sampling populations.

3. Results

Both CMUSS and CMUDS successfully processed the 665 images of the testing database. This 100% success was important for CMUDS, because it is a completely automated technique. Figure 6 shows samples of CMUSS (left column) and CMUDS (right column) segmentation. The top panels (fig. 6.A and 6.B) show the case of a straight and horizontal artery; the middle panels (fig. 6.C and 6.D) show an inclined artery; and the bottom panels (fig. 6.E and 6.F) show a curved artery. In these sample images, both CMUSS and CMUDS showed accurate LIMA tracings. This demonstrates that the snake models can deal with the anatomical variability of the arteries.

Table 3 summarizes the average IMT values measured by CMUSS (first column), by the two readers (second and third column) and by CMUDS (fourth column). CMUSS underestimated the IMT value with respect to both the readers, whereas CMUDS overestimated with respect to Reader-1 and underestimated with respect to Reader-2.

Table 4 summarizes the IMT measurement errors (first row) and absolute error (second row) form CMUSS and CMUDS compared to the readers. The best measurement accuracy (*i.e.* the mean value of the IMT bias) was shown by CMUDS when compared to Reader-2 (-0.004 mm, about 0.4% of error on the nominal IMT value of 1 mm). The lower accuracy was shown by CMUSS when compared to Reader-2 (-0.045 mm, about 4.5% of the nominal IMT value). CMUSS IMT estimates were found statistically different from those of Reader-1 ($p < 0.04$), but not from Reader-2 ($p > 0.4$). CMUDS IMT values were not different from the readers' values (p always higher than 0.2). The measurement reproducibility (*i.e.* the standard deviation of the IMT bias) was always lower for CMUDS, both when compared to Reader-1 ($p < 2.6\ 10^{-4}$) and Reader-2 ($p < 1.6\ 10^{-4}$). Hence, CMUDS measurements were overall more reproducible than CMUSS.

Figure 7 reports the IMT measurement bias for CMUSS (fig. 7.A and 7.B) and CMUDS (fig. 7.C and 7.D). The top panels are relative to Reader-1 and the bottom to Reader-2. The black line overlaid to the histogram bars represents the error cumulative function. Figure 8 reports the

comparison between the cumulative function curves for CMUSS (dashed line) and CMUDS (continuous line). By looking at the histograms in fig. 7, it can be observed that the dispersion of the CMUDS measurement errors is lower than CMUSS. This is confirmed by the standard deviations of the IMT bias in Table 4, where the standard deviation of CMUDS is always lower than that of CMUDS. Hence, CMUDS is more reproducible than CMUSS. Reproducibility is a term used to indicate the variability of a technique in the measurement of a given quantity. Thus, reproducibility is better for the technique having the lower standard deviation of the measurement error (*i.e.*, the IMT bias).

The last row of table 4 reports the Figure-of-Merit (FoM). FoM can be thought as the percent overall agreement between the IMT measurements by the readers and the computer measured IMTs. It can be defined as:

$$FoM_{CMUSS} = 100 - \left| \frac{CMUSS_{IMT} - \text{Reader}_{IMT}}{\text{Reader}_{IMT}} \right| \cdot 100$$
$$FoM_{CMUDS} = 100 - \left| \frac{CMUDS_{IMT} - \text{Reader}_{IMT}}{\text{Reader}_{IMT}} \right| \cdot 100 \quad (5)$$

where $CMUSS_{IMT}$ is the average IMT value computed by CMUSS, $CMUDS_{IMT}$ is the average IMT value computed by CMUDS, and $Reader_{IMT}$ is the average IMT value manually measured by the readers (either Reader-1 or 2). CMUSS showed FoM equal to 98.5% compared to Reader-1 and of 94.4% to Reader-2. CMUDS showed FoM of 96.0% compared to Reader-1 and 99.6% to Reader-2. Overall, CMUDS showed the highest FoM (99.6% against Reader-2) and the best average FoM (97.8% against 96.5% of CMUSS).

Table 3 – Comparison of average IMTs between CMUSS (column one), CMUDS (column 4) and the two readers (Reader-1 and Reader-2 in middle columns)

	CMUSS	Reader-1	Reader-2	CMUDS
IMT value (mm)	0.747±0.167	0.758±0.285	0.791±0.258	0.788±0.288

Table 4 – Performance Evaluation Comparisons between CMUSS (left column) and CMUDS (right column)

	CMUSS	**CMUDS**
IMT bias (mm) w.r.t Reader-1	-0.011±0.329	0.030±0.284
IMT bias (mm) w.r.t Reader-2	-0.045±0.317	-0.004±0.273
IMT abs. err. (mm) w.r.t Reader-1	0.245±0.219	0.199±0.205
IMT abs. err. (mm) w.r.t Reader-2	0.227±0.226	0.180±0.205
FoM (%) w.r.t Reader-1	98.5%	96.0%
FoM (%) w.r.t Reader-2	94.4%	99.6%

Figure 9 reports the Bland-Altmann plots for CMUSS (fig. 9.A and 9.C) and CMUDS (fig. 9.B and 9.D) with respect to the readers's intima-media thickness values. Bland-Altmann plots are very useful in clinical applications when comparing the measurement of the technique under testing to the measurements obtained by the technique considered the best (which is usually called the "golden standard"). In our application, the golden standard was the set of measurements made by the readers, whereas the techniques under testing were CMUDS and CMSS. The horizontal axis of the Bland-Altmann plots report the average IMT value between the golden standard and the technique under testing. The vertical axis reports the difference of the golden standard and testing technique IMT values. If, for example, a testing technique had a measurement bias, then the cloud of dots would show a trend. This is the case of CMUSS (left column of fig. 9): the Bland-Altmann plots report a negative trend for higher IMT values. This means that CMUSS tends to underestimation when IMT has values higher than 1 mm. The CMUDS graphs, conversely, show good accordance with manual measurements.

4. Discussion

In this paper we benchmarked the constrained our snake mode with the most performing conventional snake model for the far carotid wall segmentation and IMT measurement. The main innovation of this paper is the design of the automated constrained based dual snake model (CMUDS) and its clinical evaluation. This system is unique and novel in the medical imaging scenario for the following primary reasons:

a) Dual Snake System: two deformable parametric models (one for the LI and one for the MA) are initialized simultaneously and converge simultaneously in successive steps.
b) Constrained Paradigm: the LI and MA profiles are constrained during the evolution process.
c) Automation: the entire system is completely automated, that include: CCA recognition, ROI estimation, Snake initialization, Snake Evolution and Convergence;
d) External Energy: this term utilizes high-performance edge snapper called FOAM [11] compared to conventional gradient methodologies. This prevents bleeding and premature collapses.

No other methodologies that we are aware of use a Dual Snake system for LIMA interface computation and IMT measurement. Usually, as in CMUSS, snake-based methods use the snake sequentially in time, by first running it for LI interface computation, followed by MA computation. The evolution of the snakes is, therefore, independent. Our system can be considered as a Dual Snake, because our LIMA snakes evolve simultaneously and are constrained by each other. This constraint prevents the snakes from bleeding or collapsing. The effect of the mutual constraint can be better appreciated by looking at fig. 10. We implemented CMUDS on our database by relaxing the constraints. Figure 10.A shows one sample of CMUDS LIMA segmentation with constraints removed. The white arrow indicates a region in which the LI snake collapsed on the MA snake. The constrained version of CMUDS (fig. 10.B) showed accurate segmentations and without collapsing.

CMUDS showed overall performance that was better than CMUSS. First of all, CMUDS was statistically more reproducible compared to CMUSS. Also, the overall FoM of CMUDS was higher than that of CMUSS (97.8% for CMUDS vs. 96.5% for CMUSS). Also, we found 125 images in which CMUSS clearly showed inaccurate LIMA segmentations. Figure 11 shows two examples of inaccurate CMUSS LIMA tracings, compared to CMUDS. The white arrows in fig. 11.A and 11.C point to portions of the LIMA profiles by CMUSS that are inaccurate (the ground truth tracings by Reader-1 are shown by dashed yellow line for comparison). In fig. 11.A the $CMUSS_{MA}$ profile is traced too close to the LI and it is not placed on the actual MA interface. In fig. 11.C, the LI snake was trapped by lumen noise (which, in this image is represented by blood rouleaux) and it is distant from the reference LI interface. On the contrary, Figures 11.B and 11.D shows the stability of CMUDS tracings.

The suboptimal performance of CMUSS has been solved by CMUDS because of the constraints between the evolving LIMA curves. In fact, the external energy term linking the LI to the MA prevents the snakes from collapsing (*i.e.* from having a too low distance as in fig. 11.A) or from bleeding (*i.e.* from having a too high distance, as in fig. 11.C). Therefore, we believe that CMUDS represents a major improvement in the snake-based techniques for carotid LIMA segmentation.

The overall superior performance of CMUDS is also depicted by the Bland-Altmann plots. In fact, CMUSS (fig. 9.A and 9.C) showed bias for higher IMT values and had a marked tendency to underestimate the IMT (Table 3). We double-checked all the images corresponding to dots that were below the bottom dashed line in fig. 9.A and 9.C (the bottom dashed line represents the mean IMT bias minus one standard deviation). In total, we checked 125 images. In all those images (100% of the cases) the under-estimation was caused by a collapsing of the snakes: in 81 images (about 65%) the LI snake collapsed on the MA snake (*i.e.* the MA snake was correctly in correspondence of the actual MA border); in 37 images (about 30%) the MA snake collapsed on the LI snake (*i.e.* the LI snake was correctly positioned on the actual LI border); and in the remaining 7 images (about 5%) both the snakes collapsed and none was in correspondence of the actual

interfaces. Hence, all these error conditions were originated by the lack of mutual constraints between the snakes.

The best performing snake-based algorithms that were published in literature were by Cheng *et al.* [24] and Delsanto *et al.* (29). All these techniques segmented the LIMA profiles independently thereby more susceptible to noise. Cheng *et al.* proposed a zip-lock snake. Such snake originates from two points that must be placed no more than 1 mm away from the interface one wants to segment (28). Therefore, manual interaction was required in order to start the snake convergence. Delsanto *et al.* proposed an automated method for the snake initialization. Such method was based on a user-independent procedure for the carotid lumen detection that was based on signal analysis (29, 33, 48). All the pixels that were considered as possibly belonging to the carotid lumen constituted a mask, which was then used to locate the distal artery wall. The LIMA snakes were initialized by using the vertical gradients (48) of the image. This means that the intensity changes in the image were computed in the vertical direction, which was orthogonal to CCA of LIMA interfaces, normally running horizontal in the ultrasound scan.

However, the direct comparison of CMUSS and CMUDS performance with respect to previous snake-based techniques is not straightforward for the following reasons:

- *Distance Metric*. Cheng *et al.* (28) and Delsanto *et al.* (29) used the root mean squared error as a performance metric and the Euclidean distance as IMT distance metric. We measured that the Euclidean distance, but due to the morphology of the arterial shape such as horizontal vs. curved, there can be a bias in results up to 35% due to shape changes (see the different carotid morphologies in fig. 6).
- *Multi-institutional dataset*. We validated CMUSS and CMUDS on a 665 images database coming from five different Institutions. The images were acquired using four different ultrasound OEM scanners. The pixel density varied from a minimum of 11 pixels/mm to a maximum of 17 pixels/mm, hence if we consider an IMT value of 1 mm, its representation varied from 11 pixels to 17 pixels in our dataset. Previous snake-based

algorithms were validated on single-institutional datasets and, therefore, with fixed pixel density.

- *Multi-ethnic dataset*. The database we used comprised images coming from four different European countries (Mediterranean basin) and one Asian country (Hong-Kong). This is an important difference, because it has been shown that different ethnic groups have lipid percentage around the heart and the major vessel layers (49) that could differ up to about 42 cm^3 (when comparing, for instance, Chinese from African American). Hence, ethnicity might influence the echographic appearance of the carotid, thus constituting a further challenge for the snake system.
- *Atherosclerotic and normal arteries*. Our dataset comprised normal and pathological vessels.

All the above-mentioned differences between our testing dataset and previous studies also justify the high IMT error standard deviation we measured. Our IMT measurement reproducibility was of the order of 0.2 mm, which is about 20% of the nominal IMT value. The best performing computer methods for IMT measurement showed reproducibility of about 0.02 mm (about 2% of the IMT normal value). We attribute this increased variability at the above-mentioned characteristics of our testing image set. In fact, we computed the average difference between the IMT measurements between the two readers as: 0.033 ± 0.291 mm. Therefore, the reproducibility between the two readers was of the same order of magnitude as the IMT bias of CMUSS and CMUDS.

5. Conclusions

We benchmarked a dual-snake constrained snake system for the carotid wall segmentation and IMT measurement (which we called as CMUDS) against a single snake unconstrained system (which we called CMUSS). We showed that the mutual constrain between the LI and MA snakes increases the

overall system performance with greater clinical stability. Particularly, the reproducibility of CMUDS was statistically better than CMUSS. CMUDS, which is fully automated, had 100% of success on a large dataset of 665 images coming from different clinical centers.

The potentialities of CMUDS represent a valuable clinical asset in large epidemiological studies.

References

[1] Organization WH. Cardiovascular disease [WWW document]. URL http://www.who.int/cardiovascular_diseases/en/

[2] Badimon JJ, Ibanez B, Cimmino G. Genesis and dynamics of atherosclerotic lesions: implications for early detection. Cerebrovasc Dis. 2009;27 Suppl 1:38-47.

[3] Walter M. Interrelationships among HDL metabolism, aging, and atherosclerosis. Arterioscler Thromb Vasc Biol. 2009;29:1244-50.

[4] Kampoli AM, Tousoulis D, Antoniades C, Siasos G, Stefanadis C. Biomarkers of premature atherosclerosis. Trends Mol Med. 2009;15:323-32.

[5] van der Meer IM, Bots ML, Hofman A, del Sol AI, van der Kuip DA, Witteman JC. Predictive value of noninvasive measures of atherosclerosis for incident myocardial infarction: the Rotterdam Study. Circulation. 2004;109:1089-94.

[6] Ogata T, Yasaka M, Yamagishi M, Seguchi O, Nagatsuka K, Minematsu K. Atherosclerosis found on carotid ultrasonography is associated with atherosclerosis on coronary intravascular ultrasonography. J Ultrasound Med. 2005;24:469-74.

[7] Polak JF, Pencina MJ, Herrington D, O'Leary DH. Associations of edge-detected and manual-traced common carotid intima-media thickness measurements with framingham risk factors: the multi-ethnic study of atherosclerosis. Stroke. 2011;42:1912-6.

[8] Polak JF, Pencina MJ, Meisner A, Pencina KM, Brown LS, Wolf PA, D'Agostino RB, Sr. Associations of Carotid Artery Intima-Media Thickness (IMT) With Risk Factors and Prevalent Cardiovascular Disease: Comparison of Mean Common Carotid Artery IMT With Maximum Internal Carotid Artery IMT. J Ultrasound Med. 2010;29:1759-68.

[9] von Sarnowski B, Ludemann J, Volzke H, Dorr M, Kessler C, Schminke U. Common carotid intima-media thickness and framingham risk score predict incident carotid atherosclerotic

plaque formation: longitudinal results from the study of health in Pomerania. Stroke. 2010;41:2375-7.

[10] Wendelhag I, Wiklund O, Wikstrand J. Arterial wall thickness in familial hypercholesterolemia. Ultrasound measurement of intima-media thickness in the common carotid artery. Arterioscler Thromb. 1992;12:70-7.

[11] Polak JF, Funk LC, O'Leary DH. Inter-reader differences in common carotid artery intima-media thickness: implications for cardiovascular risk assessment and vascular age determination. J Ultrasound Med. 2011;30:915-20.

[12] Touboul PJ, Prati P, Scarabin PY, Adrai V, Thibout E, Ducimetiere P. Use of monitoring software to improve the measurement of carotid wall thickness by B-mode imaging. J Hypertens Suppl. 1992;10:S37-41.

[13] Touboul PJ, Vicaut E, Labreuche J, Belliard JP, Cohen S, Kownator S, Pithois-Merli I. Design, baseline characteristics and carotid intima-media thickness reproducibility in the PARC study. Cerebrovasc Dis. 2005;19:57-63.

[14] Molinari F, Zeng G, Suri JS. A state of the art review on intima-media thickness (IMT) measurement and wall segmentation techniques for carotid ultrasound. Computer Methods and Programs in Biomedicine. 2010;100:201-21.

[15] Faita F, Gemignani V, Bianchini E, Giannarelli C, Ghiadoni L, Demi M. Real-time measurement system for evaluation of the carotid intima-media thickness with a robust edge operator. J Ultrasound Med. 2008;27:1353-61.

[16] Liguori C, Paolillo A, Pietrosanto A. An automatic measurement system for the evaluation of carotid intima-media thickness. Instrumentation and Measurement, IEEE Transactions on. 2001;50:1684-91.

[17] Stein JH, Korcarz CE, Mays ME, Douglas PS, Palta M, Zhang H, et al. A semiautomated ultrasound border detection program that facilitates clinical measurement of ultrasound carotid intima-media thickness. J Am Soc Echocardiogr. 2005;18:244-51.

[18] Rossi AC, Brands PJ, Hoeks AP. Automatic recognition of the common carotid artery in longitudinal ultrasound B-mode scans. Med Image Anal. 2008;12:653-65.

[19] Rossi AC, Brands PJ, Hoeks AP. Automatic localization of intimal and adventitial carotid artery layers with noninvasive ultrasound: a novel algorithm providing scan quality control. Ultrasound Med Biol. 2010;36:467-79.

[20] Gutierrez MA, Pilon PE, Lage SG, Kopel L, Carvalho RT, Furuie SS. Automatic measurement of carotid diameter and wall thickness in ultrasound images. Computers in Cardiology. 2002;29:359-62.

[21] Liang Q, Wendelhag I, Wikstrand J, Gustavsson T. A multiscale dynamic programming procedure for boundary detection in ultrasonic artery images. IEEE Trans Med Imaging. 2000;19:127-42.

[22] Stoitsis J, Golemati S, Nikita KS. A Modular Software System to Assist Interpretation of Medical Images—Application to Vascular Ultrasound Images. Instrumentation and Measurement, IEEE Transactions on. 2006;55:1944-52.

[23] Meiburger KM, Molinari F, Acharya UR, Saba L, Rodrigues P, Liboni W, et al. Automated carotid artery intima layer regional segmentation. Phys Med Biol. 2011;56:4073-90.

[24] Molinari F, Meiburger KM, Zeng G, Nicolaides A, Suri JS. CAUDLES-EF: Carotid Automated Ultrasound Double Line Extraction System Using Edge Flow. J Digit Imaging. 2011.

[25] Destrempes F, Meunier J, Giroux MF, Soulez G, Cloutier G. Segmentation in ultrasonic B-mode images of healthy carotid arteries using mixtures of Nakagami distributions and stochastic optimization. IEEE Trans Med Imaging. 2009;28:215-29.

[26] Golemati S, Stoitsis J, Sifakis EG, Balkizas T, Nikita KS. Using the Hough transform to segment ultrasound images of longitudinal and transverse sections of the carotid artery. Ultrasound Med Biol. 2007;33:1918-32.

[27] Golemati S, Tegos TJ, Sassano A, Nikita KS, Nicolaides AN. Echogenicity of B-mode sonographic images of the carotid artery: work in progress. J Ultrasound Med. 2004;23:659-69.

[28] Cheng DC, Schmidt-Trucksass A, Cheng KS, Burkhardt H. Using snakes to detect the intimal and adventitial layers of the common carotid artery wall in sonographic images. Comput Methods Programs Biomed. 2002;67:27-37.

[29] Delsanto S, Molinari F, Giustetto P, Liboni W, Badalamenti S, Suri JS. Characterization of a Completely User-Independent Algorithm for Carotid Artery Segmentation in 2-D Ultrasound Images. Instrumentation and Measurement, IEEE Transactions on. 2007;56:1265-74.

[30] Loizou CP, Pattichis CS, Pantziaris M, Tyllis T, Nicolaides A. Snakes based segmentation of the common carotid artery intima media. Med Biol Eng Comput. 2007;45:35-49.

[31] Xu C, Prince JL. Snakes, shapes, and gradient vector flow. IEEE Trans Image Process. 1998;7:359-69.

[32] Molinari F, Zeng G, Suri JS. Intima-media thickness: setting a standard for completely automated method for ultrasound. IEEE Transaction on Ultrasonics Ferroelectrics and Frequency Control. 2010;57:1112-24.

[33] Molinari F, Liboni W, Giustetto P, Badalamenti S, Suri JS. Automatic computer-based tracings (ACT) in longitudinal 2-D ultrasound images using different scanners. Journal of Mechanics in Medicine and Biology. 2009;9:481-505.

[34] Molinari F, Pattichis C, Zeng G, Saba L, Acharya U, Sanfilippo R, et al. Completely Automated Multi-resolution Edge Snapper (CAMES) inverted question mark A New Technique for an Accurate Carotid Ultrasound IMT Measurement: Clinical Validation and Benchmarking on a Multi-Institutional Database. IEEE Trans Image Process. (in press).

[35] Zhen Y, Jasjit S, Yajie S, Janer R. Four image interpolation techniques for ultrasound breast phantom data acquired using Fischer's full field digital mammography and ultrasound system (FFDMUS): a comparative approach. Image Processing, 2005 ICIP 2005 IEEE International Conference on. Vol 2, 2005:II-1238-41.

[36] Loizou CP, Pattichis CS, Christodoulou CI, Istepanian RSH, Pantziaris M, Nicolaides A. Comparative evaluation of despeckle filtering in ultrasound imaging of the carotid artery. Ultrasonics, Ferroelectrics and Frequency Control, IEEE Transactions on. 2005;52:1653-69.

[37] Demi M, Paterni M, Benassi A. The first absolute central moment in low-level image processing. Comput Vis Image Und. 2000;80:57-87.

[38] Suri JS, Haralick RM, Sheehan FH. Greedy algorithm for error correction in automatically produced boundaries from low contrast ventriculograms. Pattern Anal Appl. 2000;3:39-60.

[39] Loizou CP, Pantziaris M, Pattichis MS, Kyriacou E, Pattichis CS. Ultrasound image texture analysis of the intima and media layers of the common carotid artery and its correlation with age and gender. Comput Med Imaging Graph. 2009;33:317-24.

[40] Loizou CP, Pattichis CS, Nicolaides AN, Pantziaris M. Manual and automated media and intima thickness measurements of the common carotid artery. IEEE Trans Ultrason Ferroelectr Freq Control. 2009;56:983-94.

[41] Otsu N. A Threshold Selection Method from Gray-Level Histograms. Systems, Man and Cybernetics, IEEE Transactions on. 1979;9:62-6.

[42] Williams DJ, Shah M. A Fast Algorithm for Active Contours and Curvature Estimation. Cvgip-Imag Understan. 1992;55:14-26.

[43] Loizou CP, Pattichis CS, Pantziaris M, Tyllis T, Nicolaides A. Quality evaluation of ultrasound imaging in the carotid artery based on normalization and speckle reduction filtering. Med Biol Eng Comput. 2006;44:414-26.

[44] Saba L, Montisci R, Molinari F, Tallapally N, Zeng G, Mallarini G, Suri JS. Comparison between manual and automated analysis for the quantification of carotid wall by using sonography. A validation study with CT. Eur J Radiol. (in press).

[45] Rocha R, Campilho A, Silva J, Azevedo E, Santos R. Segmentation of the carotid intima-media region in B-Mode ultrasound images. Image and Vision Computing. 2010;28:614-25.

[46] Saba L, Sanfilippo R, Tallapally N, Molinari F, Montisci R, Mallarini G, Suri JS. Evaluation of carotid wall thickness by using Computed Tomography (CT) and semi-automated ultrasonographic software. Journal for Vascular Ultrasound. (in press).

[47] Petroudi S, Loizou C, Pantziaris M, Pattichis M, Pattichis C. A fully automated method using active contours for the evaluation of the intima-media thickness in carotid US images. Conf Proc IEEE Eng Med Biol Soc.2011:8053-7.

[48] Delsanto S, Molinari F, Giustetto P, Liboni W, Badalamenti S. CULEX-completely user-independent layers extraction: ultrasonic carotid artery images segmentation. Conf Proc IEEE Eng Med Biol Soc. 2005;6:6468-71.

[49] Brinkley TE, Hsu FC, Carr JJ, Hundley WG, Bluemke DA, Polak JF, Ding J. Pericardial fat is associated with carotid stiffness in the Multi-Ethnic Study of Atherosclerosis. Nutr Metab Cardiovasc Dis.21:332-8.

Figure Legends

Figure 1

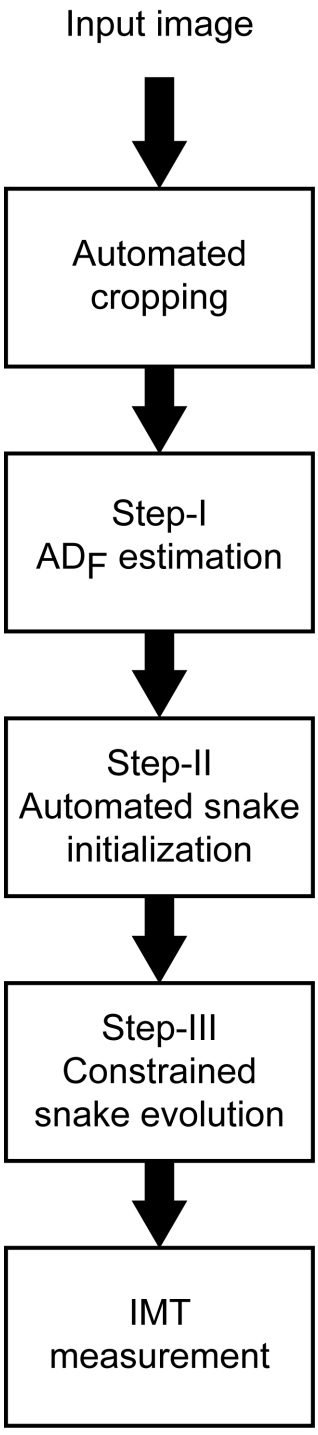

Flow-chart of the Carotid Measurement Using Dual Snake (CMUDS) system.

Figure 2

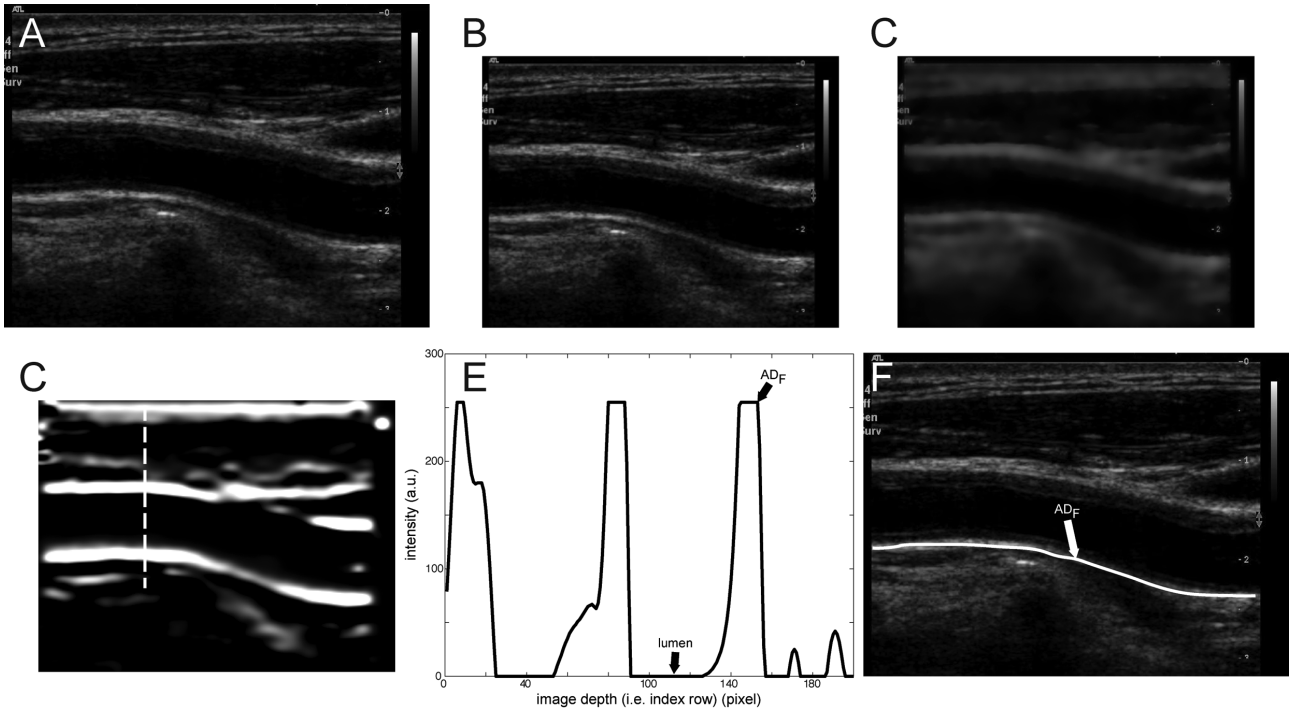

Schematic representation of the automated far adventitia (AD_F) tracing. A) Original B-Mode image. B) Down-sampled image. C) Filtered image after speckle noise reduction. D) Filtered image after convolution with a first-order derivative Gaussian kernel with scale parameter σ = 8 pixels. The dashed vertical white line indicates a column of the image whose intensity profile is reported by panel E. E) Intensity profile of an image column. The AD_F is recognized as the deepest pixel whose intensity is mapped to 255 (i.e. the maximum value on the gray scale). F) Final AD_F profile.

Figure 3

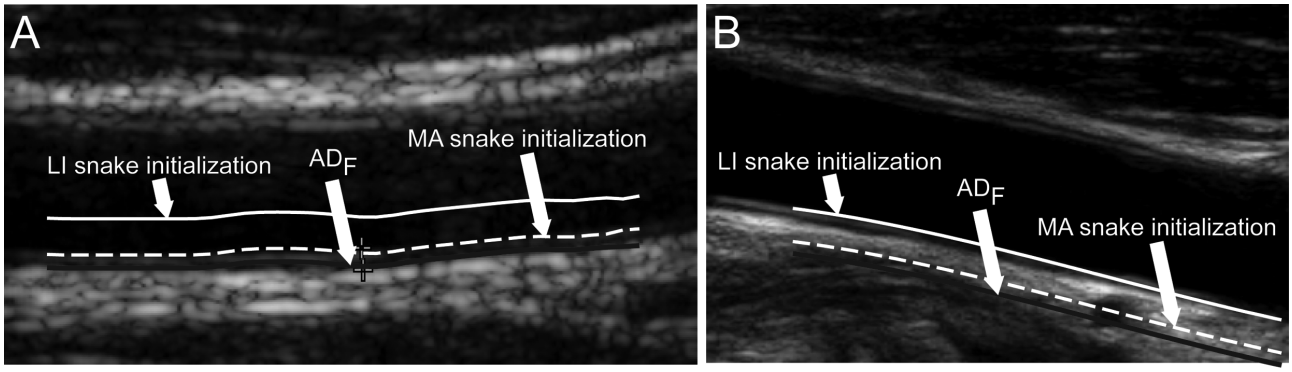

Automated initialization of the lumen-intima (LI – white line) and media-adventitia (MA – white dashed line) snakes starting from the far adventitia (AD_F – black line) profile.

Figure 4

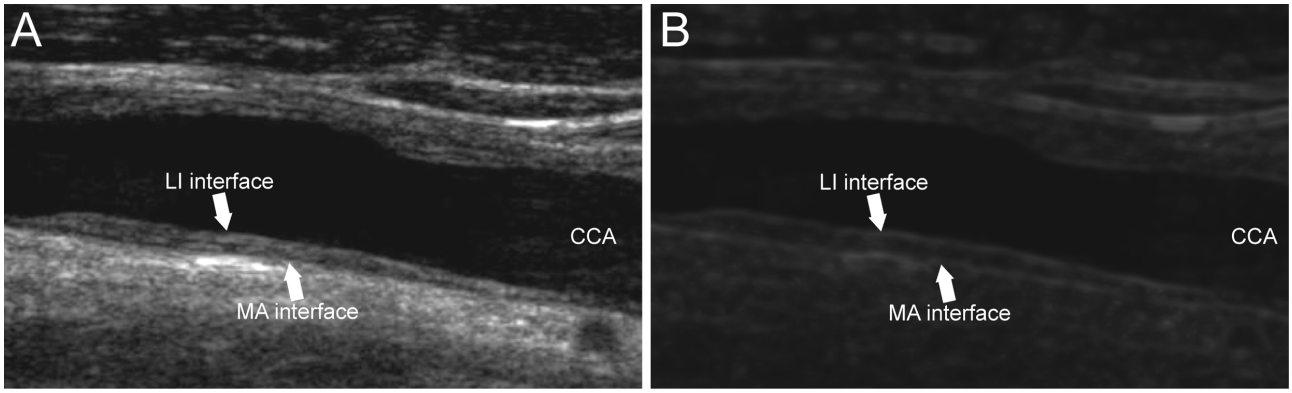

Sample of First Order Absolute Moment (FOAM) edge operator. A) Original B-Mode image. B) FOAM edge map.

(LI – lumen-intima interface; MA – media-adventitia interface; CCA – common carotid artery)

Figure 5

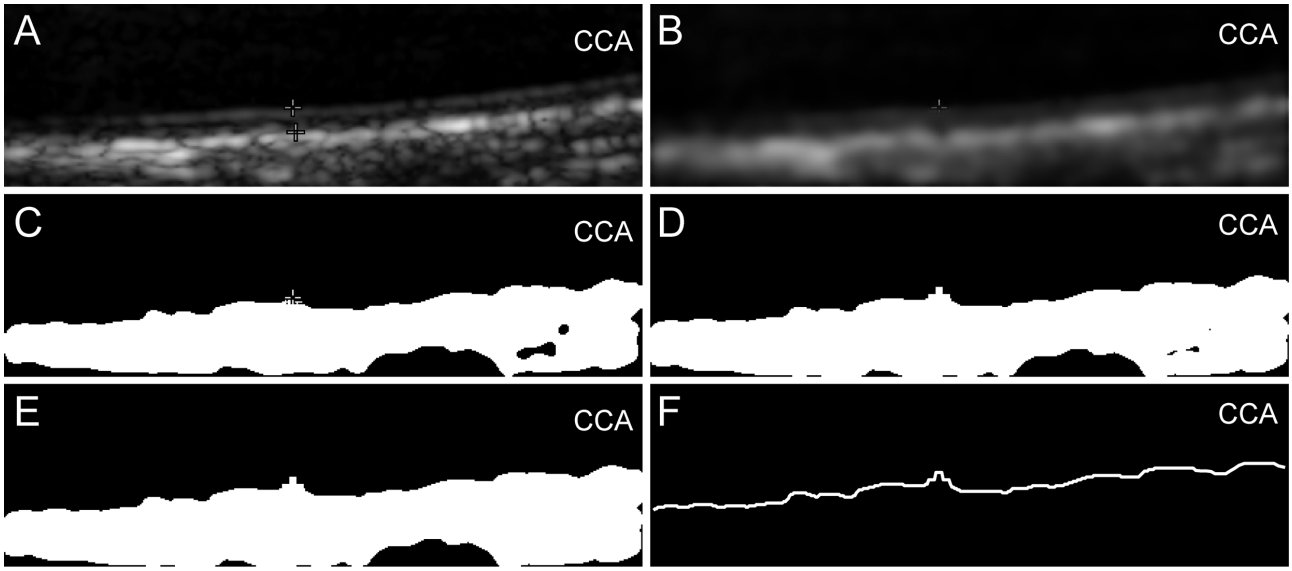

Preprocessing strategy for LI snake initialization. A) Original normalized image (manually traced ROI). B) Despeckled image. C) Binarized image. D) Image after morphological opening. E) Connected components analysis. F) Image gradient and initial LI contour.

(CCA – Common Carotid Artery)

Figure 6

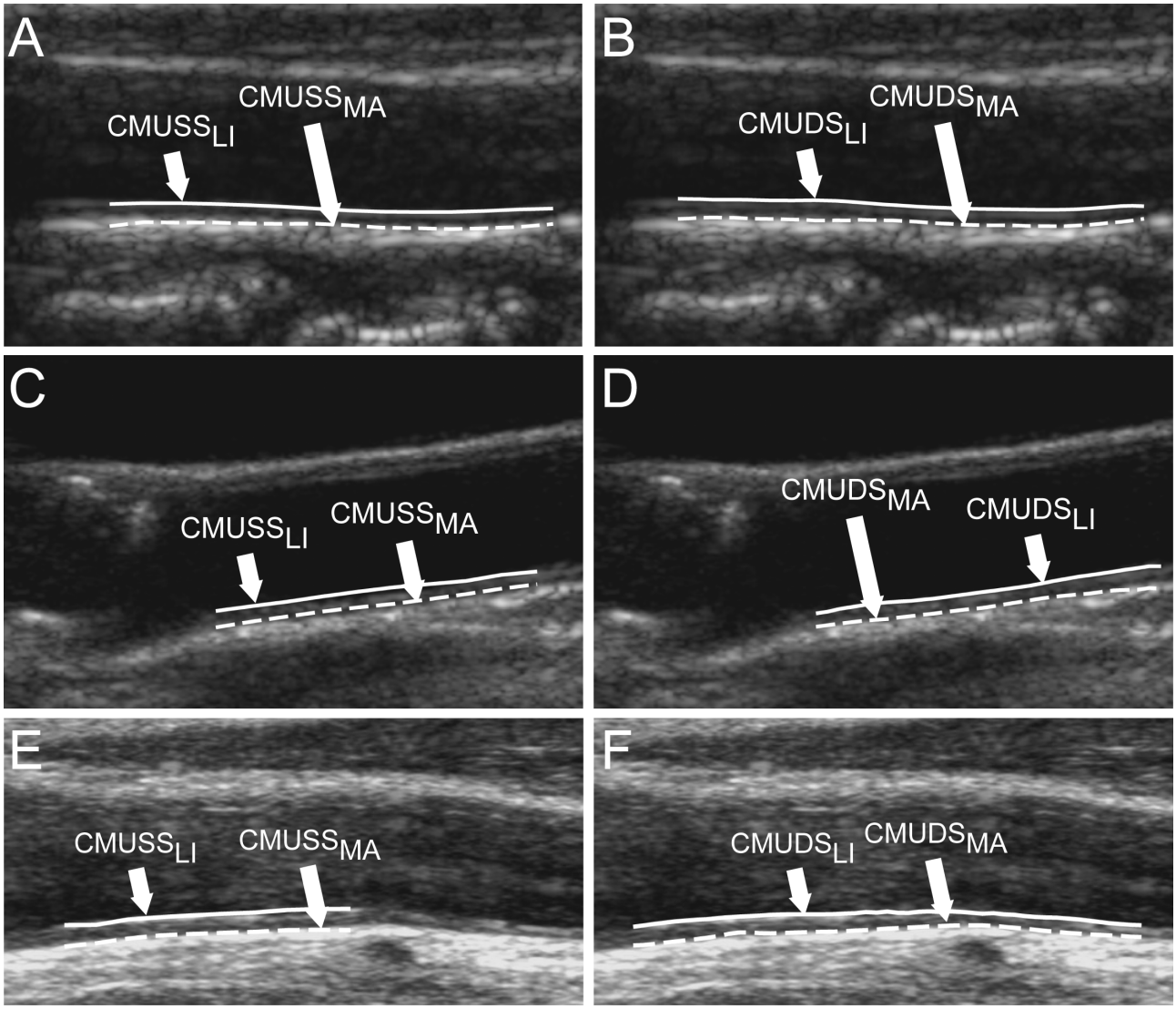

Samples of CMUSS (left column) and CMUDS LIMA tracings. Panels A and B are relative to a straight and horizontal artery, panels C and D to a inclined artery, and panels E and F to a curved artery. In these images, CMUSS and CMUDS both showed accurate tracings.

($CMUSS_{LI}$ – lumen-intima tracing by CMUSS; $CMUSS_{MA}$ – media-adventitia tracing by CMUSS; $CMUDS_{LI}$ – lumen-intima tracing by CMUDS; $CMUDS_{MA}$ – media-adventitia tracing by CMUDS)

Figure 7

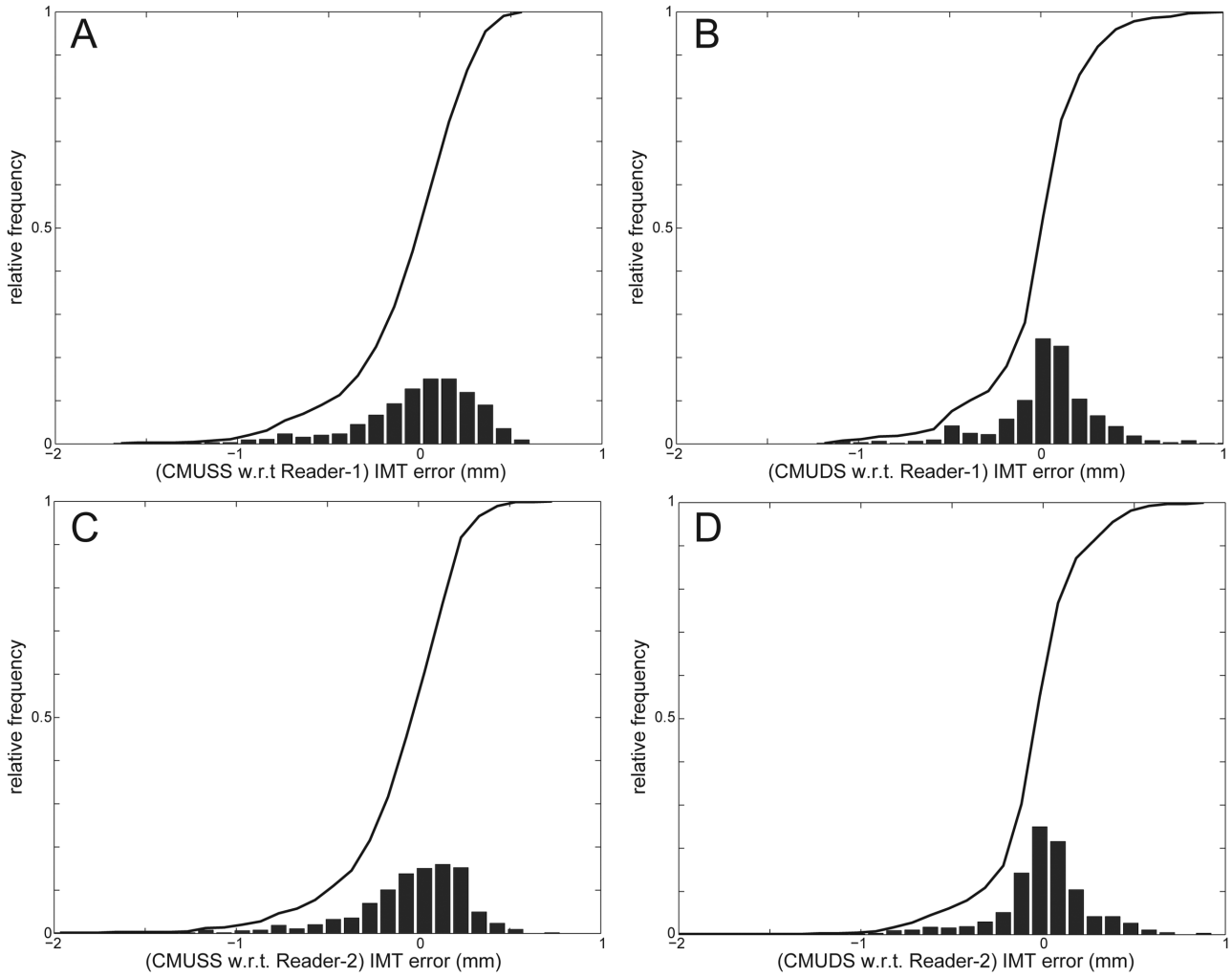

Histogram representation of the IMT measurement error (bias) for CMUSS (left column) and CMUDS (right column). Top panels are relative to Reader-1 (A and B), bottom panels to Reader-2 (C and D). The black line overlaid to the histograms represents the cumulative function.

Figure 8

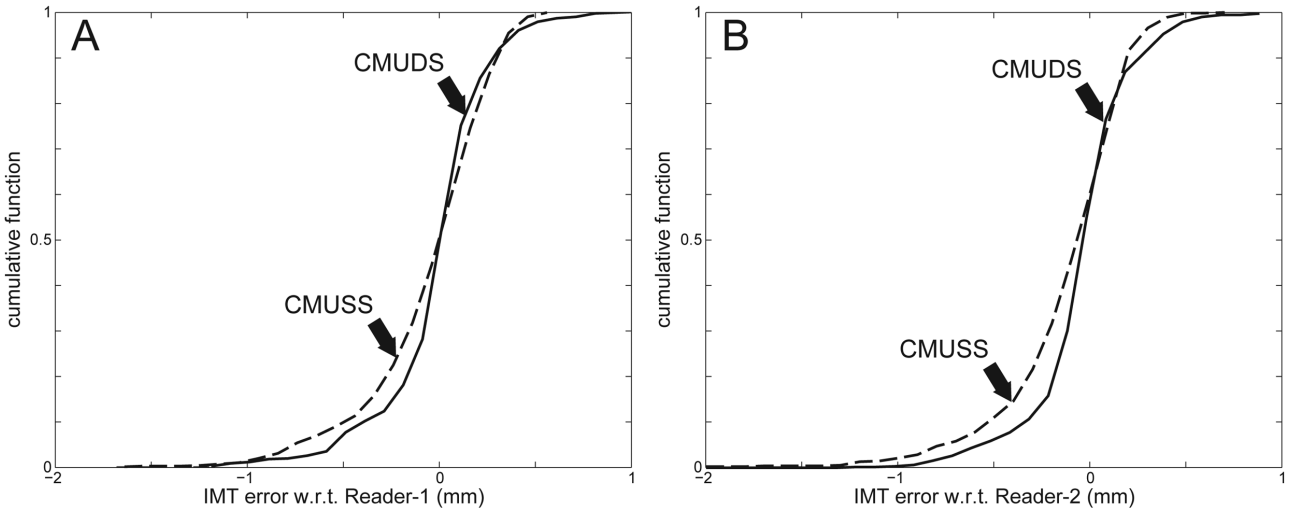

Comparison of the IMT bias cumulative functions w.r.t. Reader-1 (A) and Reader-2 (B). CMUSS cumulative functions are plotted by dashed lines, CMUDS by continuous lines.

Figure 9

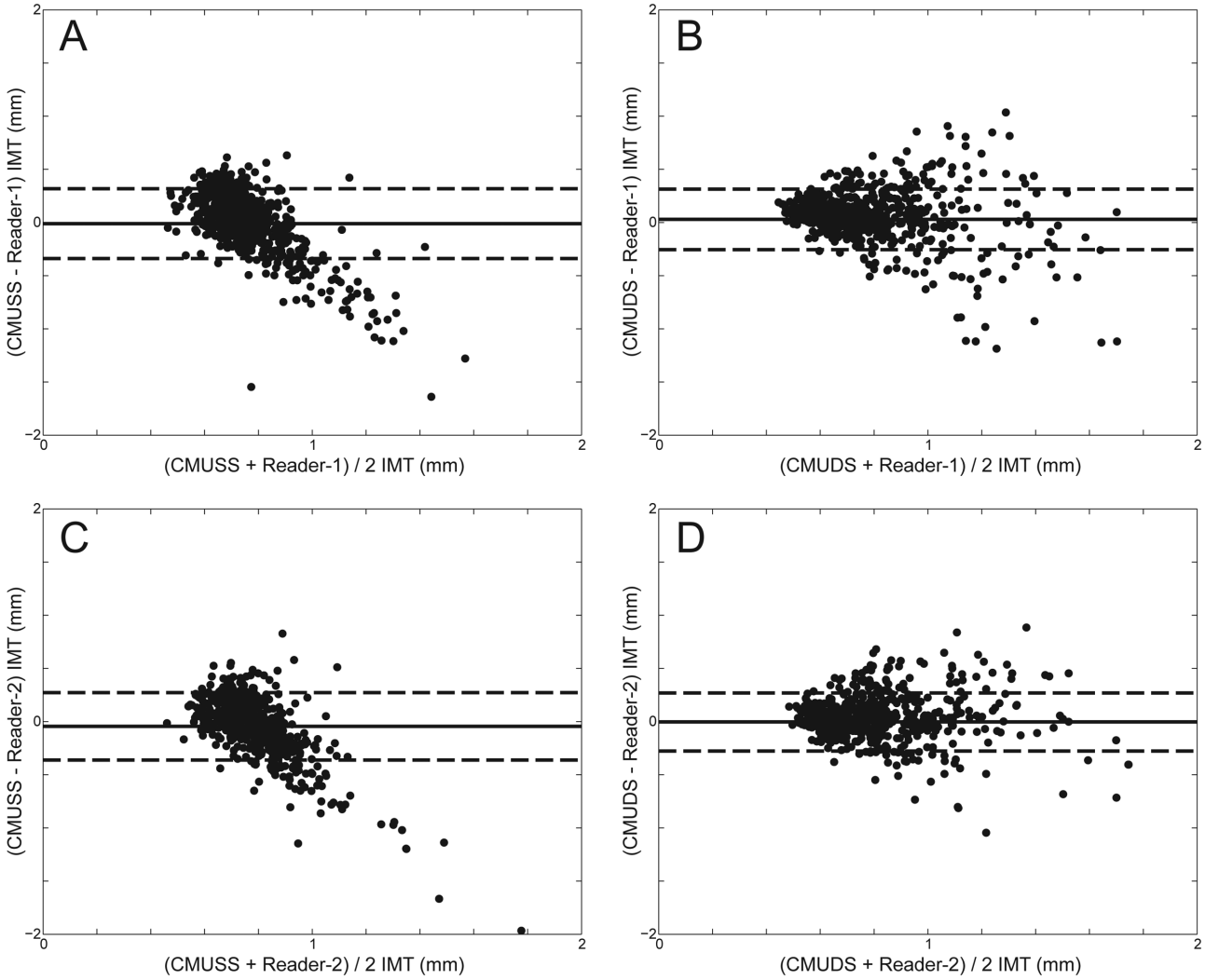

Bland-Altmann plots for CMUSS (left column) and CMUDS (right column) compared to the readers' IMT values. The top row (panels A and B) are relative to reader1, the bottom panels (C and D) to Reader-2.

Figure 10

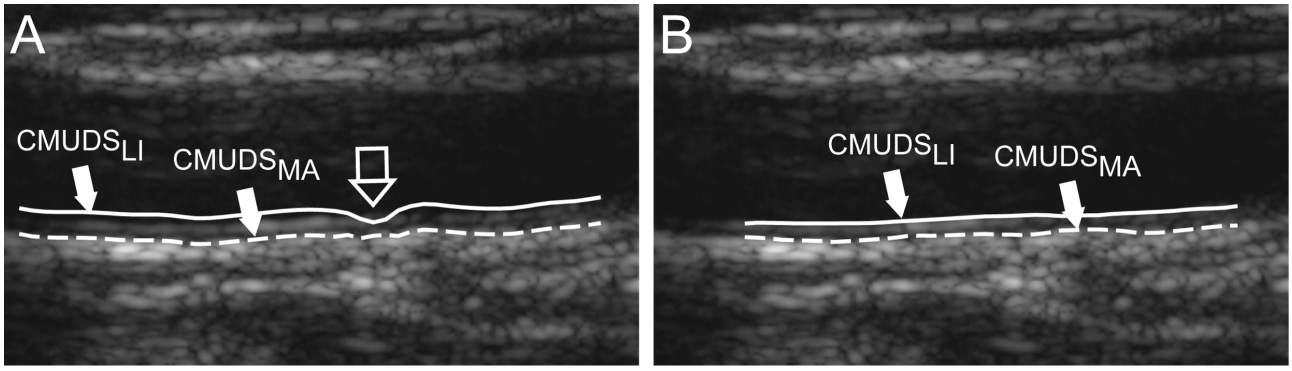

Comparison between unconstrained (panel A) and constrained CMUDS (panel B). The white arrow indicates a region where the LI snake (continuous white line) collapsed on the MA (dashed white line) due to lack of external energy.

Figure 11

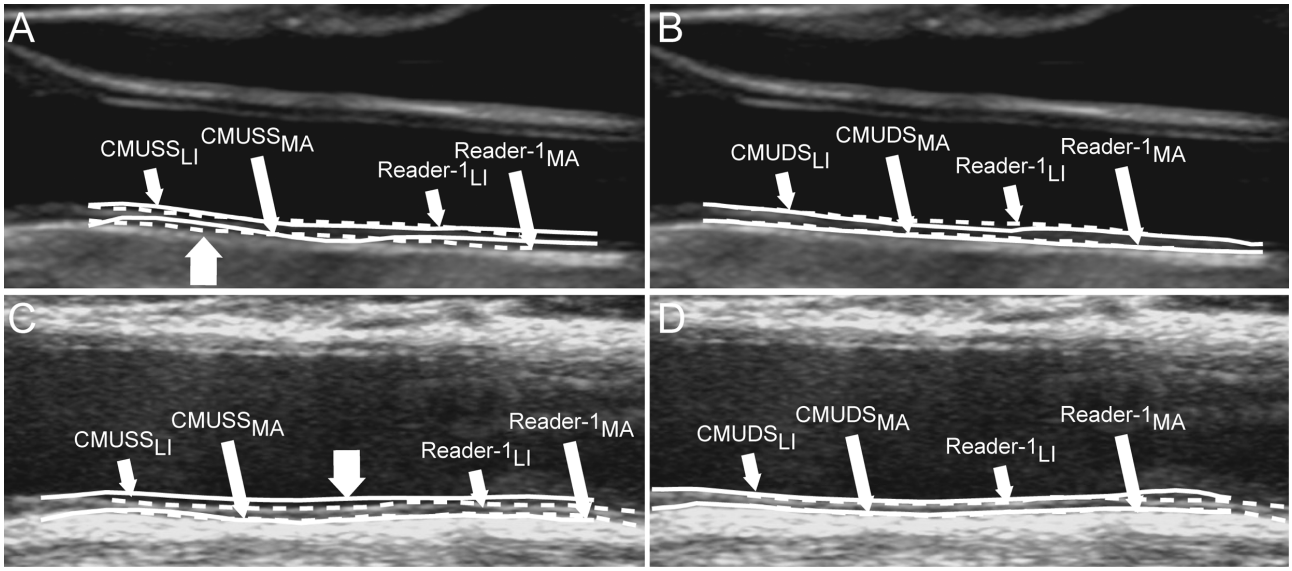

Comparison of CMUSS (left column) and CMUDS (right column) performance on two images. The computer generated LIMA are represented by white continuous lines. The manual tracings by Reader-1 are shown by white dashed lines. The white arrows in panels A and C show inaccurate CMUSS profiles.

(CMUSS$_{LI}$ – lumen-intima tracing by CMUSS; CMUSS$_{MA}$ – media-adventitia tracing by CMUSS; CMUDS$_{LI}$ – lumen-intima tracing by CMUDS; CMUDS$_{MA}$ – media-adventitia tracing by CMUDS; Reader-1$_{LI}$ – lumen-intima tracing by Reader-1; Reader-1$_{MA}$ – media-adventitia tracing by Reader-1)

List of Abbreviations

IMT	Intima-media thickness
LI	Lumen-intima
MA	Media-adventitia
CMUDS	Carotid Measurement Using Dual Snake
CMUSS	Carotid Measurement Using Single Snake
LIMA	Lumen-intima and media-adventita interfaces
AD_F	Far wall adventitia layer
ROI	Region of interest
FOAM	First-order absolute moment
CF	Conversion factor
FoM	Figure-of-Merit